Facile Synthesis of Octacalcium Phosphate Nanobelts: Growth Mechanism and Surface Adsorption Properties

Xianyan Yang,[†] Xin Gao,[†] Yilai Gan,[†] Changyou Gao,[†] Xinli Zhang,[†,‡] Kang Ting,[‡] Benjamin M. Wu,[§] and Zhongru Gou*[,†]

Zhejiang-California International NanoSystems Institute, Zhejiang University, Hangzhou 310029, People's Republic of China, Dental and Craniofacial Research Institute, School of Dentistry, University of California, Los Angeles, California 90095, and Department of Bioengineering, School of Engineering, University of California, Los Angeles, California 90095

Received: December 7, 2009; Revised Manuscript Received: March 9, 2010

A thorough understanding of the growth and surface properties of calcium−phosphate nanocrystals is essential for uncovering the mechanism by which their nanostructure interacts with other molecules. Herein, we reported a facile wet-chemical approach using cetyltrimethylammonium bromide (CTAB) for the oriented growth of octacalcium phosphate (OCP) nanobelts with a clean surface. The effect of various synthesis conditions, such as aging time, calcium salt species, CTAB, and/or other additive concentrations, on the growth of OCP nanobelts was examined. The results showed that the morphology of OCP nanobelts from a simple core to complex clusters was easily controlled by increasing aging time and CTAB concentration, whereas the nanobelt growth was heavily inhibited by a minor amount of polyaspartate (i.e., 0.03−0.12 μM). The postadsorption tests indicated the nanobelt surface was highly inert to CTAB, but had affinity to polyaspartate. Furthermore, the adsorption capability of therapeutic biphosphonate on OCP nanobelts and as-hydrolyzed/-thermolyzed HA belt-like counterparts was studied. The mechanism of dandelion-like clusters was proposed, in which the collaborative effect of CTAB vesicles and lamellar templates plays a key role. These results shed light on the underlying growth mechanism and surface adsorption of OCP nanobelt growth, as a potential new guest-species delivery/ adsorption nanomaterial.

Introduction

Biologically formed bone hard tissue, referred to as calcium phosphates (CaPs) biominerals, has intrigued the material engineering community because of the various degree of crystallographic control that is exerted during the precipitation of the biomimetic CaPs crystals.[1,2] Their structures and surface properties are attracting increasing attention and being applied to develop adsorbents for separation/purification of biomolecules[3] as well as designated drug carriers for the treatment of diseases.[4–6]

Octacalcium phosphate (OCP) is proposed as a precursor of biological apatite in bone.[7] It is believed that OCP also serves as a transient crystalline phase in which intramembranous mineralization commences.[8] Recent studies indicate that the synthetic OCP has potential application in bone defect repair, cell scaffolds, and active molecule delivery due to its bioactivity and biodegradability.[9–11] The structure of OCP is composed of alternating stacks of an "apatite layer", similar to the apatite structure, and a "hydrated layer", corresponding to the composition of brushite.[12] Since OCP possesses this unique structure that enables acidic phosphate groups (HPO_4^{2-}) to exchange various ions, it has been widely studied in interactions with organic compounds related to biological and environmental problems. For example, various dicarboxylates (i.e., succinicate, aspartate, and adipate) have been shown to readily substitute HPO_4^{2-} in the hydrated layer. Moreover, OCP's unique characteristics lend itself to be used as environmentally acceptable adsorbents, ultrasensitive gas sensors, and as a separator of proteins because of its chemical interaction with organic substances.[13–16]

The synthesis of OCP with adjustable nanostructure and surface reactivity has developed into a promising field in material chemistry.[17,18] Two typical studies have shown that the architecture of OCP can be controlled to form plate or rod nanocrystals as well as sphero-aggregate in polyaspartate (PAsp) solution or gelatin gel.[19–21] Although the controllable growth of OCP clusters has been widely studied by using polyanionic molecule mediation, the synthesis of OCP nanostructures across several length scales with a minimal level of surface contaminants still poses a challenge. Indeed, the secondary contaminant phases have not been a major focus of concern during CaP synthesis.[22,23] However, these ignored substances can drastically alter the surface property of CaP and further influence the interaction with biologically relevant molecules.[24,25] OCP crystals are typically small, extremely platy, and almost invariably twinned. It is of interest in biological and material sciences to clarify the interaction between OCP and organic molecules, which is important not only in controlling the affinity of OCP for (bio)materials but also in clarifying its role in biological mineralization. Generally, the epitaxial control by nucleation of specific crystal faces due to a precise arrangement of organic acids exposing charged functionality (usually containing acidic residues positioned to chelate cations) is crucial in influencing OCP (100) direction elongation in its formation of nanorods and plate-like crystals.[26,27] Although the OCP structure is not classified normally into compounds consisting of layers bound

* To whom correspondence should be addressed. Phone: +86 571 8697 1782. Fax: +86 571 8697 1539. E-mail: zhrgou@zju.edu.cn.
[†] Zhejiang University.
[‡] School of Dentistry, University of California.
[§] School of Engineering, University of California.

10.1021/jp911576f
Published on Web 03/19/2010

by van der Waals forces or hydrogen bonds, we would expect from structural considerations that OCP behaves more actively toward organic compounds than other CaPs and might incorporate some drug molecules into the hydrated layer. Thus, the clean OCP nanostructures would be a useful platform to understand the initial interfacial behavior with the selective molecules.[13,16,17]

In this study, we hypothesize that the cationic surfactant lamellar templates may "sandwich" the longitudinal side of the OCP plates and modulate the nanocrystal growth while its surface remains clear. Cetyltrimethylammonium bromide (CTAB), which is an extensively applied structure-directing amphiphilic small molecule, has the potential to form vesicles over critical micelle concentration (CMC) and transform lamellar structure with increasing concentration in solution.[28,29] Kumacheva et al. proposed a self-assembled gold nanorod chain structure by "coating" CTAB lamellar micelle on the longitudinal faces and polystyrenes on the transverse sides.[30] Recently, Wang et al. used the cosurfactant of CTAB and *n*-pentanol to prepare monetite nanofibers for improving the mechanical properties of biomedical composite.[31,32] However, such short fibers were heavily contaminated by surfactant in a hydrothermal approach. In this paper we proposed a wet-chemical approach to synthesize OCP nanobelts with controllable crystal growth and clean surface in a CTAB-containing aqueous solution. Hydrolysis or thermolysis of OCP leads to transformation into hydroxyapatite (HA) with belt-like nanocrystals. The surface of nanobelts exhibits a different reactive to polypeptide, CTAB, and biphosphonate. These designable surface functionality properties might have great significance in mineralization research and may lend themselves to the discovery of a new form of drug delivery.

Experimental Section

Materials. The polyaspartate (PAsp, Taihe Co., China), alendronate sodium (Sigma), high purity grade $Na_2HPO_4 \cdot 12H_2O$, $NaH_2PO_4 \cdot 2H_2O$, $Ca(CH_3COO)_2 \cdot H_2O$, $Ca(NO_3)_2 \cdot 4H_2O$, and $CaCl_2$ (BBI, Canada) were used directly. CTAB (>99.0%) was bought from Sinopharm Chemical Co., China, and was recrystallized from heated water. Deionized water used in all experiments was prepared in a three-stage Millipore Mill-Q Plus 185 purification system with a resistivity of 18.2 $M\Omega \cdot cm^{-1}$.

Synthesis of OCP Nanobelts (Route I). Synthesis of OCP nanobelts was carried out by addition of 64 mM $Ca(CH_3COO)_2$ (125 mL) (1 drop per second) into a $Na_2HPO_4-NaH_2PO_4$ solution (16 mM, 375 mL) containing CTAB (1.0 mM), at a starting pH of 5.0. The reaction in a round-bottomed flask was undertaken at 60 °C in a water bath under stirring. The white suspension was aged for 0 or 60 min and then filtered through a 0.45-μm membrane. The products were washed several times with deionized water and ethanol, and vacuum dried overnight. The reference samples of OCP synthesis were performed in the absence of CTAB with $Ca(CH_3COO)_2 \cdot H_2O$, $Ca(NO_3)_2 \cdot 4H_2O$, and $CaCl_2$, as calcium salt, respectively, while the other reaction conditions remained the same.

Effect of CTAB Concentrations on OCP Nanobelt Growth (Route II). Synthesis of OCP nanobelts was carried out at 60 °C under stirring by adding 125 mL mixing solution of CTAB and $Ca(CH_3COO)_2$ (64 mM) into a $Na_2HPO_4-NaH_2PO_4$ solution (16 mM, 375 mL) at a starting pH of 5.0. The final concentration of CTAB in the aqueous solution was 0.2−0.8 mM in different reaction batches. The resulting white suspensions were aged for 60 min and the products were then washed with deionized water and ethanol before vacuum drying.

Effect of PAsp Concentration on OCP Nanobelt Growth (Route III). When the synthesis was performed in the coexistence of CTAB (1.0 mM) and PAsp in the phosphate salt solution, the polymer was added into the phosphate solution before pH adjustment with different PAsp concentrations (i.e., 0.03 and 0.12 μM, respectively). Subsequently, the precipitates were prepared, washed, and dried by using the processes stated above.

Hydrolysis and Thermolysis Experiments (Route IV). The hydrolysis and thermolysis of OCP nanobelts were respectively carried out as follows: (1) OCP nanobelts (0.50 g) were added into an acetic acid/sodium acetate buffer with pH of 5.0 ± 0.1 and the sealed bottle was then placed in an 80 °C water bath for different time stages; (2) the crucible with OCP nanobelts was heated at 700 °C for 90 min, and then cooled naturally. The products were also washed with deionized water, followed by immersion in pure ethanol (100 mL) for 60 min, and then vacuum dried.

Surface Adsorption Experiments. The adsorption tests were performed by soaking OCP nanobelts in 0.005−0.02 mM PAsp and 0.20−0.80 mM CTAB aqueous solution at 37 °C 4 h under stirring, respectively. The nanobelts were washed with deionized water three times and dried under vacuum. The adsorption of alendronate sodium (AS) was performed by soaking 25 mg of OCP, as-hydrolyzed or as-thermolyzed nanobelts in an AS aqueous solution (200 ppm, pH 7.25, 6 mL) at 37 °C with vibration for 3 and 12 h, respectively. The AS concentrations in the supernatant solutions were then measured by a simple UV−vis spectrophotometric method (DU800, Beckman) described elsewhere.[33] Three individual tests were performed on the same batch of nanobelts. Comparative studies of averages were performed by using one way analysis of variance followed by a post hoc test (Fisher's projected least significant difference) with a statistical significance at $p < 0.05$. Similarly, to understand the effect of surface contaminant, the surface adsorption test of more OCP belts presoaked respectively in PAsp and CTAB aqueous solution was measured by changing the AS concentration while the other conditions remained the same.

Characterization. The samples were determined by Fourier transform Infrared (FTIR, Nicolet) for the phase composition. The morphology of nanobelts was determined by scanning electron microscopy (SEM, HITACHI S4800). Atomic force microscopy (AFM) observation was performed with a Nanoscope III AFM (Digital Instruments) with a silicon nitride probe. The TEM images and selected-area electron diffraction (SAED) patterns were collected on transmission electron microscopy (TEM; JEOL 2010). The ζ potential of samples (10 mg) was measured as a function of pH in 0.01 mM KCl solution, using a Zetasizer3000HSA (Malvern) equipped capillary flow cell. The nanobelts were first ground and then dispersed ultrasonically in ultrapure water. The supernatants were changed with KCl solutions by centrifugation, and subsequently the pH-adjusted KCl solution substituted for the solution after this washing procedure. The powder X-ray diffraction (XRD) analysis was carried out with the XRD diffractometer (Thermo) equipped with a monochromator in the diffracted beam. The diffraction spectra were recorded in the 2θ range from 3° to 60°, using Cu Kα radiation with a step size of 0.02°. To evaluate the lattice constant of the OCP nanocrystals, the Rietveld refinement analysis on the short and long OCP nanobelt samples (denoted as OCP-*s* and OCP-*l*, respectively) obtained from 0.4 and 0.8 mM CTAB aqueous solutions was conducted with assistance of the computer program MAUD.[34]

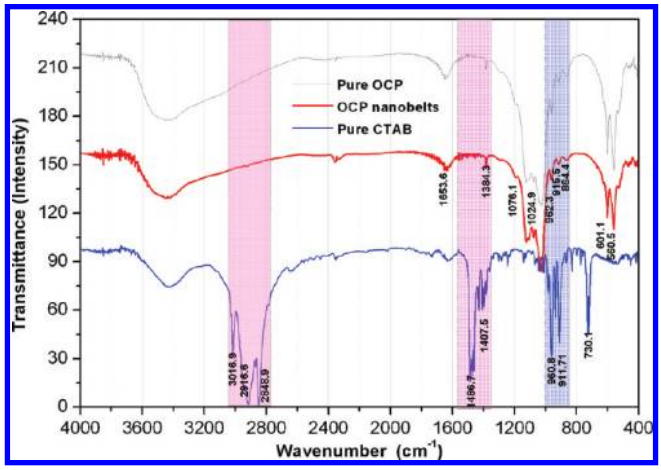

Figure 1. FTIR spectra of OCP nanobelts in comparison with pure OCP and CTAB (sharp peaks at 2848 and 2916 cm^{-1} representing C−H stretching).

Results and Discussion

Synthesis Route I (Structure and Morphology Analysis). OCP was subjected to FTIR study in order to confirm the absence of foreign molecules (i.e., CTAB) in the nanostructures, which in turn provided information about the phase purity (Figure 1). Figure 1 (red) showed its typical IR spectrum of the as-synthesized OCP,[35] with the presence of PO_4^{3-}- and/or HPO_4^{2-}-derived bands at 1076−560 cm^{-1}. The peak at 1653 cm^{-1} was associated with H_2O. However, the peaks at 3016 cm^{-1} (NH_2) and 2916, and 2848 cm^{-1} (CH_2) were scarcely detected, and the other bands at 1486−730 cm^{-1} all belonged to pure CTAB (blue).[36] The presence of a small amount of δCH (1384 cm^{-1}) in the OCP nanobelts and the pure OCP (gray) harvested from the CTAB-free aqueous medium was probably due to some ethanol adsorption in association with washing reagent.[37]

The SEM images in Figure 2a,b reveal the typical products consist of a large quantity of belt-like individuals from one core, with a macroscopic size [submillimeter in length; Figure S1, Supporting Information] during the aging stage (60 min). The high-magnification SEM images show that the width of the OCP belt is ca. 1−3 μm, and that it is quite thin (~50 nm; Figure 2c,d). There is no observable fragmentation of the crystals. This highly flexible 1D nanobelt shape is rather unusual, since OCP crystals prepared in vitro are generally in the form of short plates and rods, due to the inhibition effect of acidic biomolecules.[17−22] To our knowledge, there is no report about OCP crystals, obtained from aqueous solution or gel medium, exhibiting such fast growth rates. Usually, there is over a 2-day period time span of OCP whiskers formation in naturally derived gels.[20]

Interestingly, the AFM image displays ordered step lines parallel to (100) orientation, implying the nanobelt is possibly composed of sheet sublayers (Figure 2e). The XRD pattern (Figure 2f) confirms all of the peaks assigned to the standard OCP phase (JCPDS 26-1056). The stronger intensity (100) peak than those of other peaks (~10-fold) indicates the highly anisotropic growth of the nanocrystals. These results reflect on the excellent phase purity and a high degree of crystallinity. Panels g and h of Figure 2 show the TEM images of a typical nanobelt and its growth front. The SAED patterns can be indexed to the (100) zone axis of an orthorhombic OCP crystal (Figure 2i), suggesting a highly preferred orientation of the OCP nanobelt along this particular (100) direction.

In addition, the crystal growth of OCP is partly affected by the calcium salt species (e.g., acetate, chloride, nitrate). In our case, only belt-like OCP tens of micrometers in length could be obtained with calcium acetate as reactant in the CTAB-free precipitation process (Figure 3).

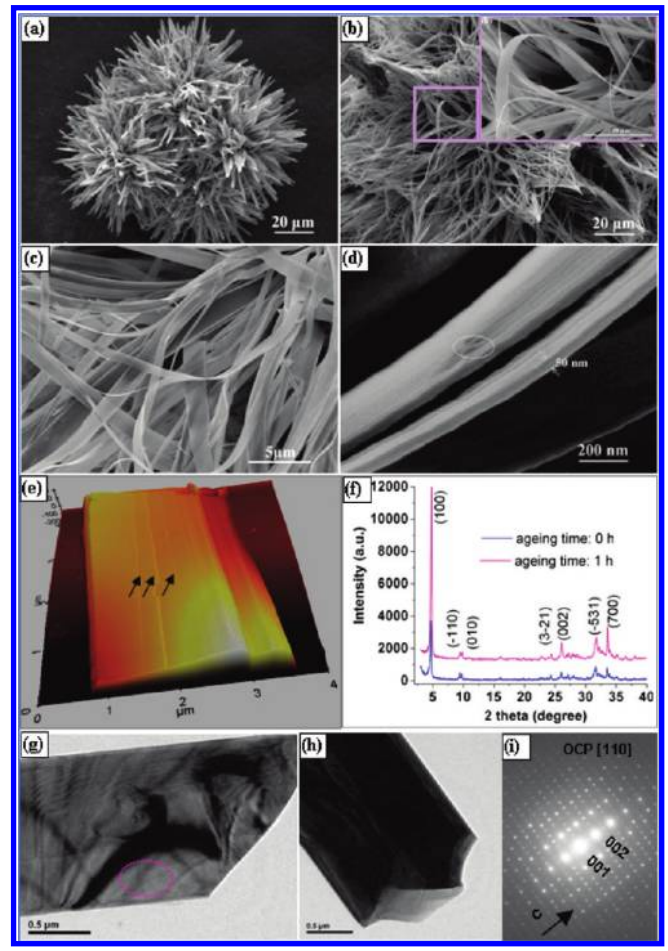

Figure 2. Morphology and structure characterization of the OCP nanobelts. SEM images of OCP nanobelts: belt clusters with aging time of 0 (a) and 1 h (b), belt surfaces (c), and belt side surfaces (d); AFM image of surface mesostructure (e); XRD patterns of OCP nanobelts with aging time of 0 and 1 h (f); TEM images of a typical belt-like OCP (g) and the growth front (h), together with SAED pattern (i). Inset in panel b: The magnified highly flexible belt appearance.

Synthesis Route II (Morphology Evolution of OCP Nanobelt Cluster). We see from Figure 4a that a limited amount of nanobelt individuals converge at the center point when adding a minor amount of CTAB (0.20 mM). With increasing CTAB up to 0.3−0.4 mM, the products evolve from radial stars to dandelion-like clusters, with more nanocrystal growth from the same core (Figure 4b,c). Notably, the length of nanobelts increases with increasing CTAB concentrations (0.6−0.7 mM) and the cluster becomes denser with respect to the packing arrangement of the nanobelts (Figure 4d,e). However, no variations of morphology, as well as nanobelt architectures, are appreciated at larger CTAB concentrations (0.8 mM; Figure 4f).

The lattice constants of OCP nanobelts precipitated in 0.4 and 0.80 mM CTAB aqueous solutions are very similar to each other, except for a slight decrease in the lattice parameter *b* (Table S1, SI). It also can be seen from the XRD patterns that the intensity of (100) peaks increases with the CTAB concentration and the strongest peaks show very limited peak shift toward a lower diffraction angle (Figure S2, SI). Moreover, the OCP exhibits the typical plate-like crystal according to the reconstructed crystal morphology via the Rietveld refinement analysis (Figure S3, SI).

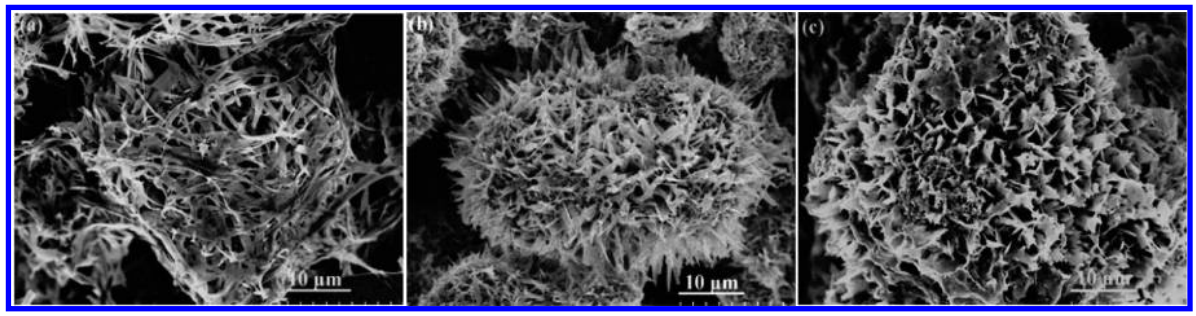

Figure 3. Morphology difference of OCP synthesized with calcium acetate (a), calcium chloride (b), and calcium nitrate (c) as calcium salt species.

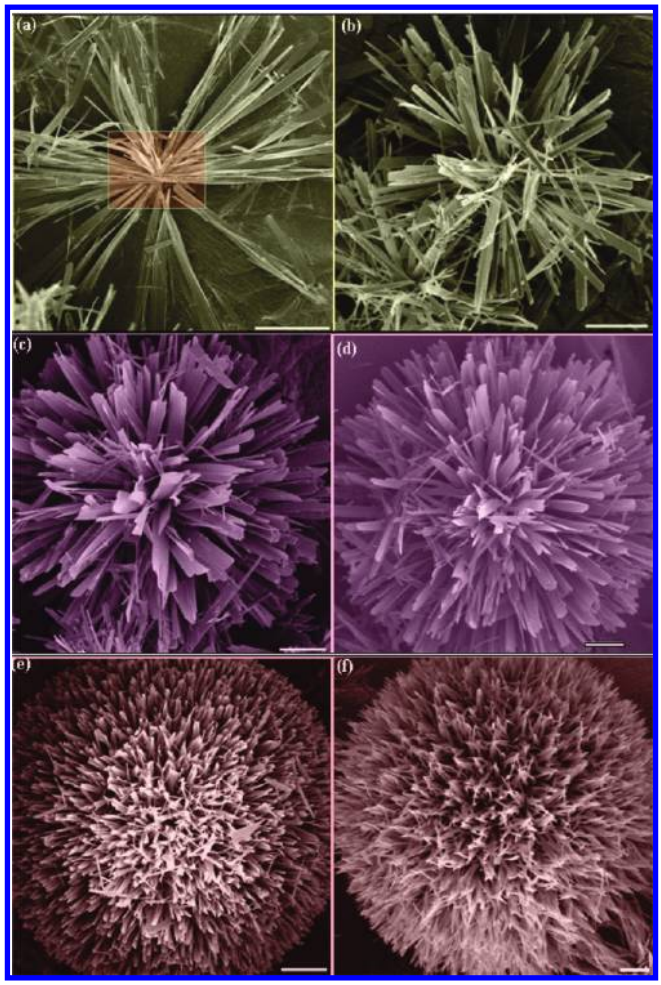

Figure 4. Morphology evolution of OCP obtained at different CTAB concentrations with 1 h of aging time: (a) 0.20, (b) 0.30, (c) 0.40, (d) 0.60, (e) 0.70, and (f) 0.80 mM. The bar is 20 μm.

Synthesis Route III (Polyanionic Molecule Inhibition on OCP Nanobelt Growth). To further explore the effect of acidic macromolecule on the belt-like OCP growth characteristic, the OCP was synthesized in the coexistence of CTAB and PAsp in the aqueous medium (Figure 5). PAsp is usually used as a nontoxic, biodegradable corrosion inhibitor for removing CaP deposit from stainless steel tubing.[38] While there is abundant literature concerning the negative control (inhibiting CaP nanocrystal growth) by PAsp at high and low concentrations,[39–41] the literature concerning positive or negative control of the coexistence of PAsp and amphiphilic molecule is comparatively scarce. In our experimental conditions, the nanobelt individuals are strongly inhibited with PAsp concentrations as low as 0.03 μM, as shown in Figure 5c,d. With increasing concentration of

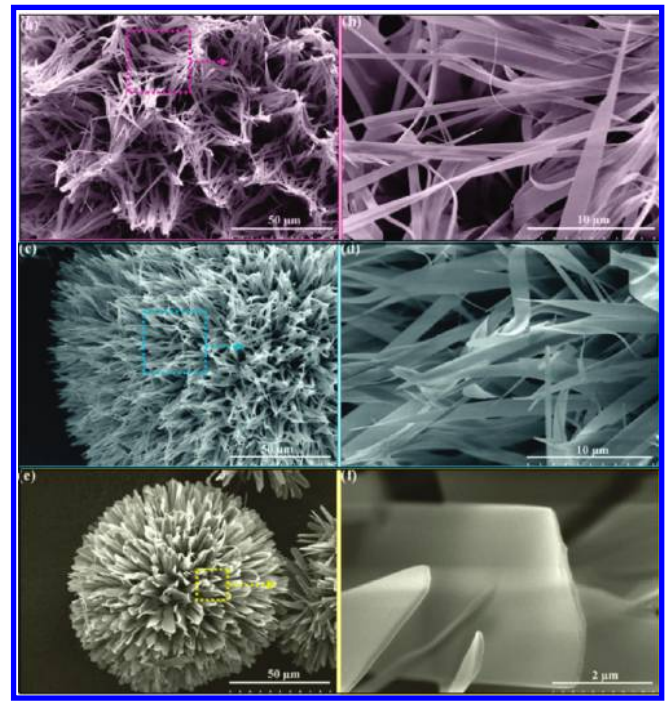

Figure 5. SEM images of OCP nanostructures synthesized in aqueous solutions in coexistence of 1.0 mM CTAB and different PAsp concentrations after 1 h of aging time: (a, b) 0 μM PAsp; (c, d) 0.03 μM PAsp; and (e, f) 0.12 μM PAsp.

PAsp up to 0.12 μM, the blade-like OCP nanocrystal of tens of micrometers in length radiating from the center region (Figure 5e,f) is approximately one-fifth of that appearing in the absence of this additive (Figure 5a,b). This coincides with other findings which indicate that the inhibition of nanocrystal is caused by adsorption of PAsp on the active crystal growth sites of OCP surfaces.[41]

Synthesis Route IV (Structure and Phase Transformation). The SEM and XRD analyses provide further insight and correlation between the morphology and phase transition of OCP nanobelts with different degrees of hydrolysis or thermolysis (Figure 6). In situ hydrolysis of OCP at 80 °C leads to phase transformation to HA after a prolonged period of time. Microscopically, the changes of crystal structure from OCP to HA seem to be accomplished with the preservation of the shape of belt-like crystals, except for some cracks at the growth front (Figure 6d), signifying the belt-like morphology is thermodynamically metastable for HA. This result is consistent with the urea-triggered blade-like OCP single crystal to rod-like HA single crystal transformation.[26] In the XRD patterns, the sample hydrolyzed for 144 h can be identified as phase-pure HA (JCPDS 09-432) compared to the partially hydrolyzed 36 h sample (Figure S4, SI). Similarly, the OCP acts as a template

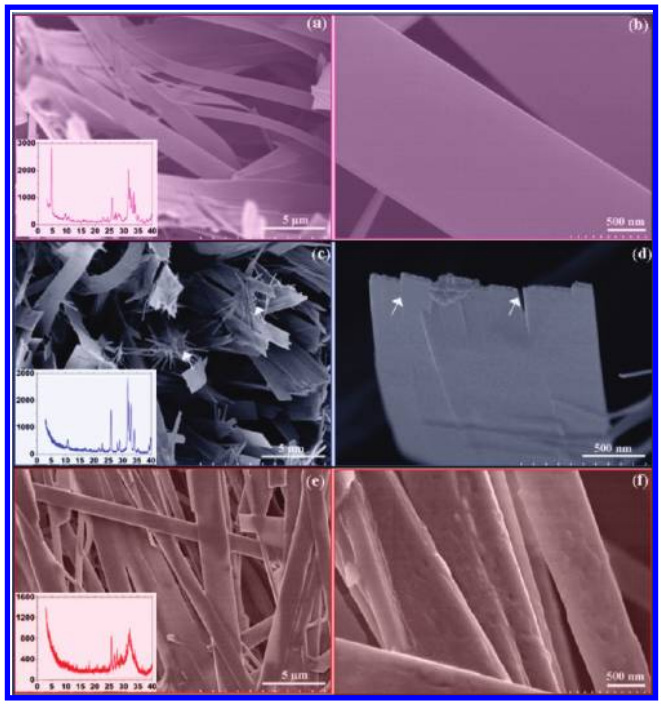

Figure 6. Morphological characteristic of nanobelts after being hydrolyzed at 80 °C for 36 (a, b) and 144 h (c, d), or thermolyzed at 700 °C for 1.5 h (e, f); XRD patterns (inset) of OCP nanobelt materials hydrolyzed at 80 °C or thermolyzed at 700 °C were transformed into HA. The arrows show the single belt crash into thinner belts from the growth front.

for phase transformation in retaining the precursor morphology during the thermolysis process (Figure 6e,f).

Potential Growth Mechanism of the OCP Nanobelt. On the basis of the above experimental results, the formation process of the nanobelt clusters can be proposed as follows (Figure 7). Unlike, the conventional CTAB reversed micelles hydrothermal process,[31] our wet-chemical process suggests that the oriented growth of OCP nanobelts is significantly dependent on CTAB concentrations. The amphiphilic small molecules initially self-assemble into spherical vesicle structures in the solution. Then, phosphate ions ($H_2PO_4^-$) are absorbed onto the positively charged headgroups (CTA^+) of the spherical vesicle through the electrostatic interactions and subsequently react with the Ca^{2+} from the added solution. Accordingly, the plate-like OCP nanocrystals grow continuously. It is noted that vesicle-like aggregates can be formed in deionized water only when the CTAB concentration reaches the CMC (~0.9 mM); however, such concentration is reduced markedly in the presence of electrolyte ions.[42] With increasing CTAB concentration the lamellar micelles structures are produced, leading to the formation of organic−inorganic−organic stacked structures. The active front of crystal nuclei will grow preferentially along a certain facet, whereas the growth of other facets is retarded due to the inhibition of lamellar micelles. On the other hand, the higher the concentration of polyanions, the more smaller sized vesicles are produced and thus the nanobelt growth slows down.[43] A significant feature of the current synthesis strategy is the oriented growth from the same core of the CTAB vesicle, together with the CTAB lamellar micelle-assisted template, which might help to retain the belt structure and result in nanobelts with a high aspect ratio. From the above results, it may be concluded the collaborative modulation of CTAB vesicles and lamellar templates plays a key role in the formation of the clean OCP long nanobelt clusters.

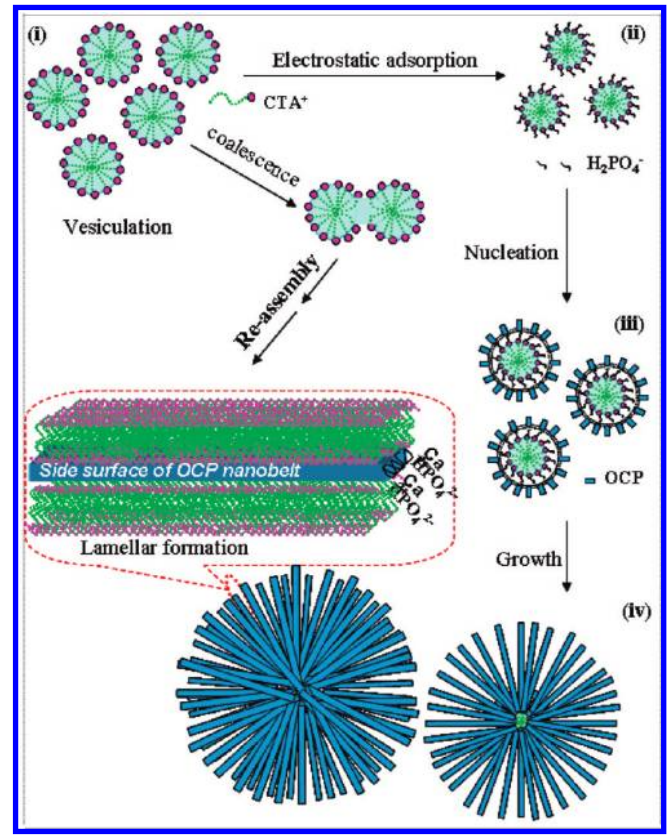

Figure 7. Schematic mechanism illustration of OCP nucleation on the CTAB vesicle preferentially protecting the longitudinal faces of the OCP nanobelts by CTAB lamellar structure template leaving the belt ends amenable to grow rapidly in the aqueous solution, without surface contamination.

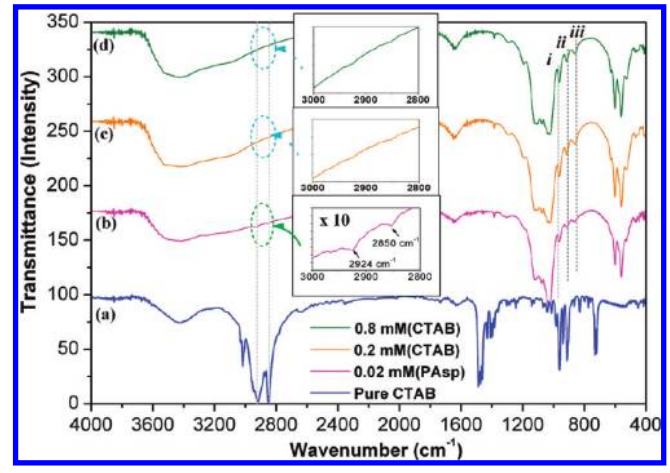

Figure 8. FTIR spectra of the treated OCP nanobelts and pure CTAB: (a) pure CTAB; (b) OCP after soaking in 0.02 mM PAsp solution; (c) OCP after soaking in 0.20 mM CTAB solution; (d) OCP after soaking in 0.80 mM CTAB solution. Insets: The highly magnified bands (×10) at 2800−3000 cm^{-1}.

Surface Adsorption Analysis. The formation mechanism of OCP nanobelts can also be supported by the FTIR spectra (Figure 1) and surface adsorption experiment (Figure 8). Figure 8 displays the FTIR spectra of OCP nanobelts after soaking in PAsp and CTAB aqueous solutions, respectively. It can be seen that the HPO_4^{2-}-derived bands at 962, 915, and 864 cm^{-1} (denoted as i, ii, and iii) are attributed to the characteristic peaks of OCP, indicating the OCP phase is almost unchanged. The weak bands at 2924 and 2880 cm^{-1} (CH_2 stretch) are both detected, implying the interaction of PAsp with OCP nanobelt

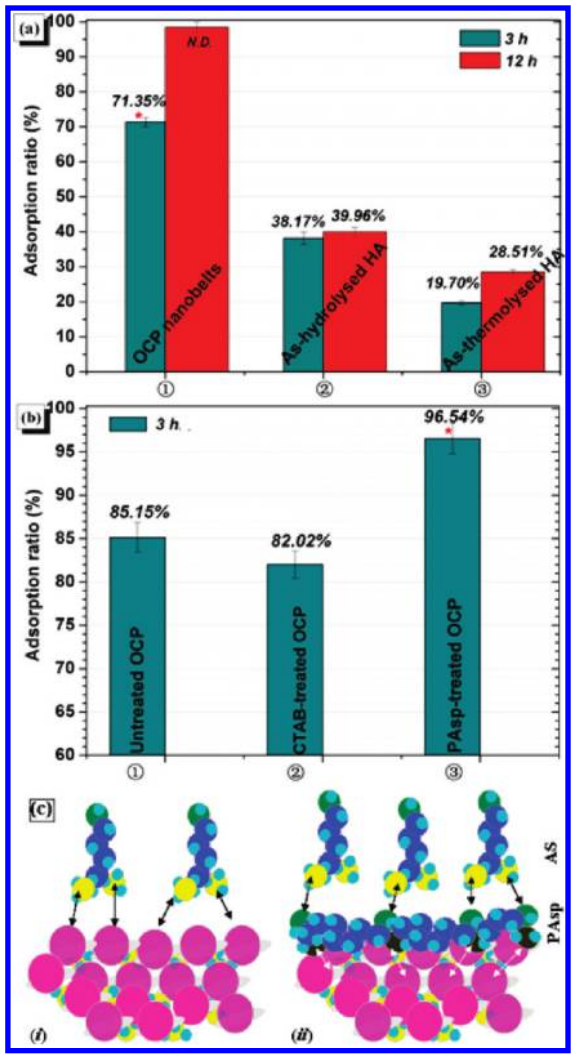

Figure 9. Adsorption ratio of AS on CaP nanobelt materials (a, b) and the schematic adsorption relationship of AS on the OCP nanobelt with and without contaminant phase (c). The asterisk identifies values not detected in the supernatant (ND) due to values being below the lower limit ($p < 0.05$).

has occurred (Figure 8b, inset). In contrast, those adsorption bands for CTAB molecules could not be detected from the CTAB-soaked OCP (Figure 8c,d). These results suggest that the anionic macromolecules are substantially adsorbed on the nanobelt surface, but such nanobelts are highly inert to the cationic surfactant.

To address specifically the affinities of biologically relevant guest molecules on the CaP nanobelt, we next questioned whether the antiresorptive drug molecules in solution could result in high adsorption capability of the nanobelts. Alendronate sodium (AS), an amino-bisphosphonate with antiresorptive potency, was chosen as a model molecule since it has been identified as having zwitterion binding to calcium cations of CaP.[44] As shown in Figure 9a, AS is preferentially adsorbed on OCP nanobelts compared with the HA ($p < 0.05$). Overall, the adsorption rate is fast during the initial period of 3 h and then levels off gradually to a quasi-steady state at 12 h, the plateau notice for AS uptake corresponding to the situation of the surface. OCP nanobelts induce nearly 2-fold and 4-fold increases in AS adsorption, compared to those on the hydrolyzed and thermolyzed HA nanobelts within 3 h, showing the superior affinity of OCP for AS. Furthermore, the effect of surface contaminant phase on AS adsorption capabilities on the pre-treated OCP nanobelts is identified (Figure 9b). As expected, the PAsp-contaminated OCP nanobelts exhibit significantly high affinity to AS within the first 3 h compared with the OCP with and without treatment by CTAB ($p < 0.05$). The most probable explanation is that chemisorption of AS takes place on PAsp molecules, via polar covalent interactions with protonated amino groups (NH_3^+) and PO_4^{3-} (Figure 9c). Meanwhile, it is likely that the interaction includes the exchange between bisphosphonate and phosphates (i.e., HPO_4^{2-}) occurring in the hydrated layer, similar to the dicarboxylate intercalation.[15] In the case of HA, however, the initial OCP precursor with hydrolysis may alter its surface property and its adsorption affinity. Specifically, since fewer calcium cations are exposed in the surface layer of the as-thermolyzed HA physisorption takes place on its surface. This may be related to the decrease in electrostatic attraction for the phosphonate groups and hydroxyl group of AS on HA. The ξ-potential of HA at pH ~7.25 was ca. twice as high as that of OCP, thereby indicating that the affinities of the two nanobelts were noticeably different (see Figure S5 in the SI). A more negative ξ-potential might lead to an increase in the energy barrier for the interaction between the nanobelt surface and AS molecules.

Viewed together, such data indicate that in the present synthetic conditions, the as-obtained nanobelts are pure OCP, without CTAB, indicating the interaction between CTAB and OCP nanocrystals is very weak and temporary. Hence, the use of positively charged small molecules, such as CTAB, to modulate OCP nanobelts presents a significant benefit. Specifically, the positively charged polar headgroups (CTA^+) assemble as vesicles and lamelles and are poorly anchored onto the nanobelt surface because of the electrostatic repulsions with the cation-rich surface.[29] This finding is crucial for high performances in designable surface functionality to further understand the interaction with biological and pharmaceutically active molecules.

Conclusions

In summary, the OCP nanobelts without surface contaminants were synthesized by a new small molecule-assisted wet-chemical method. The nonabsorbed small molecule surfactant (i.e., CTAB) has a key role in modulating crystallite anisotropic growth of long belt-like nanostructures. The hydrolysis and thermolysis of OCP were studied and the morphology of reformed HA products did not change significantly. Specific biphosphonate trapping phenomena observed on OCP nanobelts compared with the HA analogues potentially provide evidence for the development of new biomedical implants as well as a potentially successful therapeutic drug carrier. This straightforward and general synthetic route may be applied to obtain other calcium phosphate 1D nanostructures. Moreover, it is worth noting that such clean CaP nanostructures across several length scales in dimension will be a useful platform for a new understanding of the mechanism of specific surface functional molecules/groups mediating (de)mineralization.

Acknowledgment. This research was supported by grants from the Science and Technology Department of Zhejiang Province Foundation (2008C21058), the National Science Foundation of China (50902121), and the Zhejiang-California International Nanosystems Institute (J30802). We thank Prof. G. Han, Prof. R. Tang, and Prof. G. Lv for AFM measurement, Rietveld refinement analysis, and helpful discussion. We also acknowledge Ms. Miriam Razi for her aid in the language help.

Supporting Information Available: Optical microscopy images of the belts, XRD patterns, reconstructed crystal morphology, and ξ-potential measurements. This material is available free of charge via the Internet at http://pubs.acs.org.

References and Notes

(1) Kniep, R.; Simon, P. *Top. Curr. Chem.* **2007**, *270*, 73.

(2) Wang, L.; Guan, X.; Yin, H.; Moradian-Oldak, J.; Nancollas, G. H. *J. Phys. Chem. C* **2008**, *112*, 5892.

(3) Benmoussa, A.; Loiseau, P. R.; Mikou, M.; Lacout, J. L. *Chromatographia* **1996**, *42*, 177.

(4) Matsumoto, T.; Okazaki, M.; Inoue, M.; Hamada, Y.; Taira, M.; Takahashi, J. *Biomaterials* **2002**, *23*, 2241.

(5) Josse, S.; Faucheux, C.; Soueidan, A.; Grimandi, G.; Bujoli, B.; Bouler, J.-M. *Adv. Mater.* **2004**, *16*, 1423.

(6) Nancollas, G. H.; Tang, R.; Phipps, P. J.; Henneman, Z.; Gulde, S.; Wu, W.; Mangood, A.; Russell, R. G. G.; Ebetino, F. H. *Bone* **2006**, *38*, 617.

(7) Brown, W. E.; Eidelman, N.; Tomazic, B. *Adv. Dent. Res.* **1987**, *1*, 306.

(8) Crane, N. J.; Popescu, V.; Morris, M. D.; Steenhuis, P.; Ignelzi, M. A., Jr. *Bone* **2006**, *39*, 434.

(9) Honda, Y.; Anada, T.; Kamakura, S.; Morimoto, S.; Kuriyagawa, T.; Suzuki, O. *Tissue Eng., Part A.* **2009**, *15*, 1965.

(10) Shelton, R. M.; Liu, Y.; Cooper, P. R.; Gbureck, U.; German, M. J. *Biomaterials.* **2006**, *27*, 2874.

(11) Kamakura, S.; Nakajo, S.; Suzuki, O.; Sasano, Y. *J. Biomed. Mater. Res.* **2004**, *71A*, 299.

(12) Brown, W. E.; Smith, J. P.; Lehr, J. R.; Frazier, A. W. *Nature* **1962**, *196*, 1048.

(13) Aoki, S.; Nakayama, H.; Sakamoto, K.; Yamaguchi, S.; Suganuma, K. *J. Phys. Chem. Solids* **2004**, *65*, 465.

(14) Sakamoto, K.; Yamaguchi, S.; Kaneno, M.; Fujihara, I.; Satoh, K.; Tsunawaki, Y. *Thin Solid Films* **2008**, *517*, 1354.

(15) Nakahira, A.; Aoki, S.; Sakamoto, K.; Yamaguchi, S. *J. Mater. Sci.: Mater. Med.* **2001**, *12*, 793.

(16) Markovic, M. Octacalcium phosphate carboxylates. In *Octacalcium Phosphate*; Chow, L. C., Eanes, E. D., Eds.; Karger, Basel, 2001; pp77−93.

(17) Iijima, M.; Moradian-Oldakb, J. *J. Mater. Chem.* **2004**, *14*, 2189.

(18) Suzuki, O.; Kamakura, S.; Katagiri, T. *J. Biomed. Mater.Res., Part B* **2006**, *77B*, 201.

(19) Göbel, C.; Simon, P.; Buder, J.; Tlatlik, H.; Kniep, R. *J. Mater. Chem.* **2004**, *14*, 2225.

(20) Teshima, K.; Sakurai, M.; Lee, S.; Yubuta, K.; Ito, S.; Suzuki, T.; Shishido, T.; Endo, M.; Oishi, S. *Cryst. Growth Des.* **2009**, *9*, 650.

(21) Bigi, A.; Boanini, E.; Walsh, D.; Mann, S. *Angew. Chem., Int. Ed.* **2002**, *41*, 2163.

(22) Zyman, Z.; Epple, M.; Rokhmistrov, D.; Glushko, V. *Materialwiss. Werkstofftech.* **2009**, *40*, 297.

(23) Iijima, M.; Moriwaki, Y.; Takagi, T.; Moradian-Oldak, J. *J. Cryst. Growth* **2005**, *38*, 202.

(24) Grossl, P. R.; Inskeep, W. P. *Geochim. Cosmochim. Acta* **1992**, *56*, 1955.

(25) Tang, R.; Darragh, M.; Orme, C. A.; Huan, X.; Hoyer, J. R.; Nancollas, G. H. *Angew. Chem., Int. Ed.* **2005**, *44*, 2.

(26) Tseng, Y.-H.; Mou, C.-Y.; Chan, J. C. C. *J. Am. Chem. Soc.* **2006**, *128*, 6909.

(27) Falini, G.; Gazzano, M.; Ripamonti, A. *J. Mater. Chem.* **2000**, *10*, 535.

(28) Lamont, R. E.; Ducker, W. A. *J. Am. Chem. Soc.* **1998**, *120*, 7602.

(29) Zhao, F.; Du, Y.; Yang, P.; Li, X.; Tang, J. *Sci. China, Ser. B: Chem.* **2005**, *48*, 101.

(30) Nie, Z.; Fava, D.; Kumacheva, E.; Zou, S.; Walker, G. C.; Rubinstein, M. *Nat. Mater.* **2007**, *6*, 609.

(31) Wang, Y.; Lai, C.; Wei, K.; Tang, S. *Mater. Lett.* **2005**, *59*, 1098.

(32) Wei, K.; Lai, C.; Wang, Y. *J. Mater. Sci.* **2007**, *42*, 5340.

(33) Taha, E. A.; Youssef, N. F. *Chem. Pharm. Bull.* **2003**, *51*, 1444.

(34) Lutterotti, L.; Glalanella, S. *Acta Mater.* **1998**, *46*, 101.

(35) Flower, B.; Markovic, M.; Brown, W. E. *Chem. Mater.* **1993**, *5*, 1417.

(36) Campbell, R. A.; Parker, S. R. W.; Day, J. P. R.; Bain, C. D. *Langmuir* **2004**, *20*, 8740.

(37) del Arco, M.; Carriazo, D.; Gutiérrez, S.; Martín, C.; Rives, V. *Phys. Chem. Chem. Phys.* **2004**, *6*, 465.

(38) Littlejohn, F.; Sáez, A. E.; Grant, C. S. *Ind. Eng. Chem. Res.* **1998**, *37*, 2691.

(39) Bigi, A.; Boanini, E.; Bracci, B.; Falini, G.; Rubini, K. *J. Inorg. Biochem.* **2003**, *95*, 291.

(40) Tao, J.; Zhou, D.; Zhang, Z.; Xu, X.; Tang, R. *PNAS* **2009**, *106*, 22096.

(41) Bigi, A.; Bracci, B.; Panzavolta, S.; Iliescu, M.; Plouet-Richard, M.; Werckmann, J.; Cam, D. *Cryst. Growth Des.* **2004**, *4*, 141.

(42) Mirgorodskaya, A. B.; Zakharova, L. Ya.; Valeeva, F. G.; Zakharov, A. V.; Rizvanova, L. Z.; Kudryavtseva, L. A.; Harlampidi, H. E.; Konovalov, A. I. *Russ. Chem. Bull., Int. Ed* **2007**, *10*, 2000.

(43) Chen, W.; Chen, H.; Hu, J.; Yang, W.; Wang, C. *Colloids Surf., A* **2006**, *278*, 60.

(44) Fernández, D.; Vega, D.; Goeta, A. *Acta Crystallogr.* **2003**, *C59*, m543.

JP911576F